Modelling of the scatter in short fatigue cracks growth kinetics in relation with the polycrystalline microstructure

Graciela Bertolino, V. Doquet, M. Sauzay

Modelling of the scatter in short fatigue cracks growth kinetics in relation with the polycrystalline microstructure

G. Bertolino[a,*], V. Doquet[a], M. Sauzay[b]

[a]*LMS, UMR CNRS 7649, CNRS, Ecole Polytechnique, 91128 Palaiseau, France*
[b]*CEA, DEN-DMN-SRMA, CEA/Saclay, 91191 Gif-sur-Yvette Cedex, France*

Abstract

Finite element computations of the stresses ahead of a tortuous microcrack in a polycrystal (including crack flanks friction) are coupled with simulations of crystallographic crack growth based on discrete dislocations dynamics. An incubation period for crack growth beyond grain boundaries is introduced. The model reproduces the shape of experimental crack growth curves obtained on 316LN stainless steel and the decrease in arrest periods at grain boundaries as the crack grows. It predicts a large scatter in growth rates related to the variety of local textures. It also describes the fact that overloads allowing arrested cracks to cross the grain boundaries can make small cycles damaging.

Keywords: Small cracks; Dislocations; Mixed-mode; Finite elements; Variable amplitude fatigue

1. Introduction

High-cycle fatigue is characterised by a large scatter in fatigue lives, which reflects the scatter in mechanical conditions encountered by short cracks in the early stage of their development.

The stress distribution in a polycrystal can be very heterogeneous due to the elastic anisotropy of the grains. This effect is likely to be important in copper (anisotropy factor, $a = C_{11} - C_{12}/2C_{44} \approx 3.2$), austenitic stainless steels ($a \approx 3.3$) and nickel ($a \approx 2.4$) but negligible in aluminium ($a \approx 1.2$). Moreover, the local texture influences both the ease of crack transfer beyond a grain boundary (GB) and the roughness of the crack. The effective crack driving force varies substantially with the local microstructure.

Attempts to describe this scatter by introducing random variables—for the grain size, crystal orientation, local yield stress, critical stress concentration at the head of the blocked slip band for slip transfer beyond a GB—can be found in the literature [1–2]. However, these studies do not fully take into account the roughness of the crack paths nor the mixed mode loading and ignore the heterogeneity of the stress field, which can make microcracks driving force quite different from the apparent value, computed from the applied stress field.

An attempt to model this variability is made here by coupling finite element (FE) calculations of the stresses ahead of a tortuous microcrack in a polycrystal with simulations of crack growth along slip planes based on discrete dislocations dynamics (DDD) [3,4].

Moreover, in most existing models, the resistance of a GB to crack growth is considered overcome as soon as plasticity has been activated in the next grain: either this condition is fulfilled and the crack is immediately free to grow in the next grain or it is not and the crack is considered arrested once and for all. This is not fully consistent with experimental observations. On the one hand, microcracks are often observed to stay arrested for a large number of cycles at a GB and then resume propagation (see experimental observations below). On the other hand, Ludwig et al. [5] report temporarily arrested microcracks, in spite of a well visible plastic zone in the next grain. This means that the transfer of a crack tip beyond a GB does not coincide with the activation of a slip system but may require

* Corresponding author. Tel.: +33 1 69 33 33 05; fax: +33 1 69 33 30 26.
E-mail address: bertolin@lms.polytechnique.fr (G. Bertolino).

a maturation period, as suggested by Morris et al. [6]. Such an incubation period during which a microcrack could initiate in the next grain and link with the arrested one, thus allowing further propagation, has been introduced in the present study.

In addition, low-amplitude reversed torsion tests are performed on 316LN stainless steel and microcracks development is monitored to provide data for the model.

2. Experimental observations

Stress-controlled reversed torsion tests were performed at ± 120 and ± 130 MPa on tubular specimens of 316 LN steel. The specimens were water quenched after a 1 h vacuum anneal at 1050 °C, resulting in a 50 μm austenitic mean grain size, with a few ferrite bands aligned with the tube axis. The specimens were electropolished and etched to reveal the grain boundaries before tests. The tests were periodically interrupted (every 2×10^4 cycles) for preparation of replicas, which allowed SEM observations of microcracks and tracing back of their development.

The specimen tested at ± 120 MPa was not broken at 10^6 cycles. However, one-grain-size-long crystallographic microcracks initiated close to the maximum shear planes (longitudinal and transverse) and blocked by a GB were already present at 7×10^4 cycles (less than 7% of the fatigue life). It seems thus more pertinent to focus modelling efforts on micro-propagation than on crack initiation.

Fig. 1 shows some microcracks growth kinetics obtained at ± 130 MPa (fatigue life $\approx 4\times10^5$ cycles). Fig. 1b shows the final aspect of a crack formed by coalescence of two microcracks initiated independently. Arrest periods—up to 9×10^4 cycles—are observed at some GBs (label 3 on Fig. 1a and c) while some other GBs (label w on Fig. 1a and b) are overcome almost without deceleration. Note that the arrest period shows no simple correlation with the *apparent* tilt angle of the crack path at the free surface: the arrest period at the exit face of the twin boundary, label b on Fig. 1b where the crack deflection seems very small was 8×10^4 cycles. The period needed by the right tip of the left-hand crack on Fig. 1b to enter the central grain (with an apparent tilt around 60°) and link with the left tip of the right-hand crack was 9×10^4, in spite of the high stress concentration due to the proximity of two crack tips.

Zhai and Wilkinson [7] underlined that both the tilt and twist angles of the crack plane determine the ease of crack transfer from one grain to the other. Unfortunately, even though some useful data on grain-to-grain misorientations can be obtained from EBSD mappings, the 3D orientation of the GB plane itself (and not just its trace on the free surface) has to be known in order to derive the exact tilt and twist angles at the GB. Such a measurement has not been attempted yet.

Fig. 1 shows that arrest periods constitute by far the most important fraction of the life and that the growth rate during

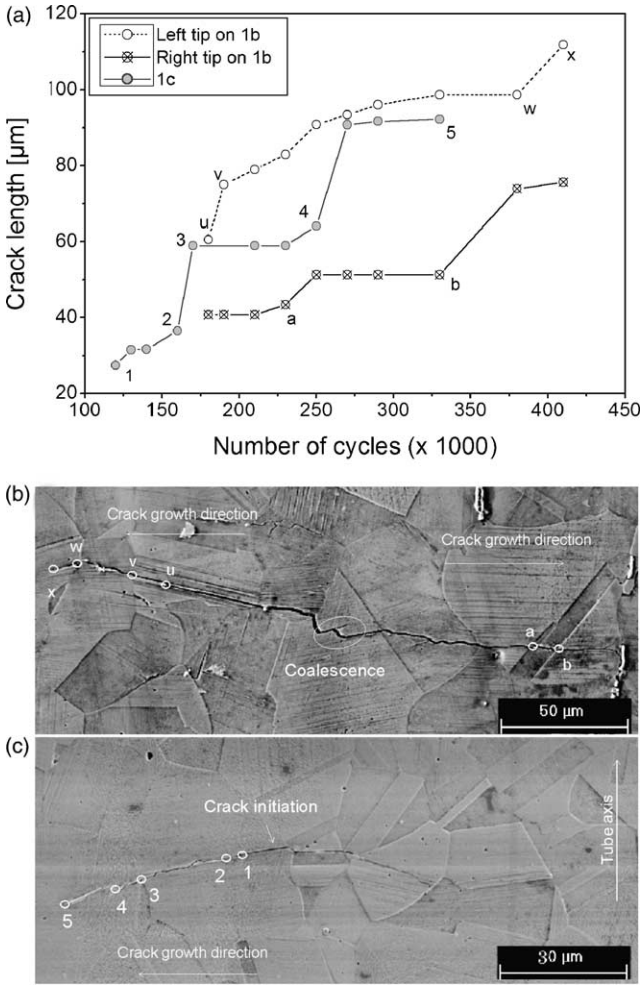

Fig. 1. Microcracks growth in reversed torsion at ± 130 MPa. a, measured kinetics; b and c, aspect of the cracks.

transgranular periods is no more than 10 Burgers vectors/cycle.

Sometimes, cracks became arrested soon after crossing a GB. This case was often associated with a large deflection of the crack plane.

Fretting debris coming out microcracks flanks were observed (Fig. 2). Similar debris—clearly different from

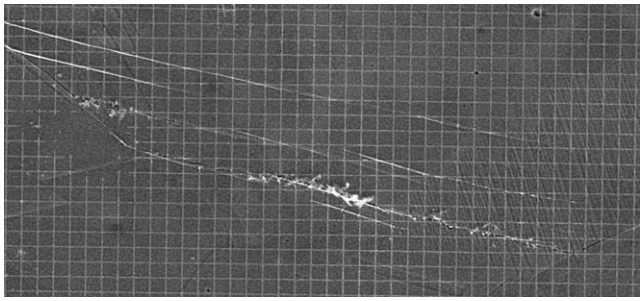

Fig. 2. Fretting debris exuding from the flanks of a microcrack (the square grid pitch is 4 μm).

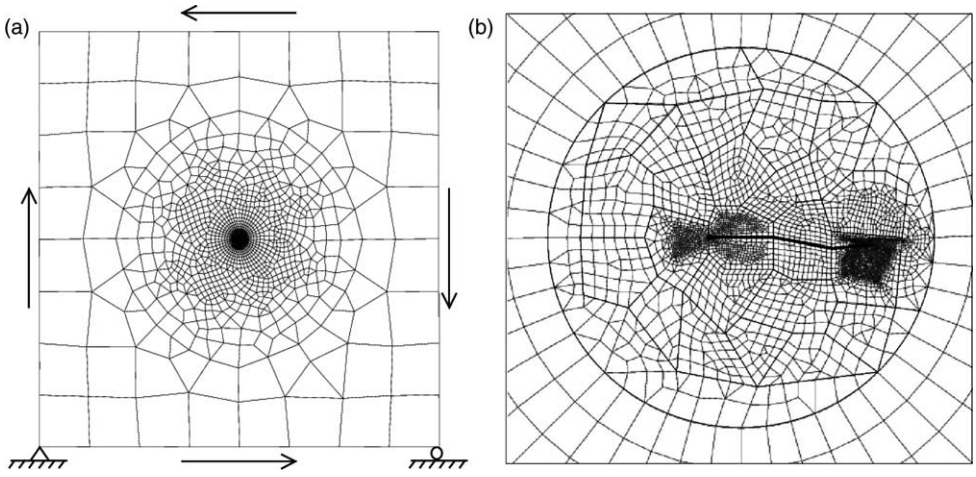

Fig. 3. Finite element mesh and boundary conditions a, entire mesh; b, details of polycristal.

classical extrusions—had also been observed along stage I microcracks in a CoNi alloy [3] and in a NiAl alloy, by Grummon et al. [8]. That is why the influence of crack flanks friction—which was described in an empirical approximate fashion in [3]—was analysed here more rigorously, using FE simulations on tortuous cracks (see below).

For the stress levels investigated, the transition toward Stage II propagation occurred most often when the cracks were three grain-size-long. In the following, Stage I crack growth is thus modelled over three grains.

3. Principle of the simulations

3.1. Finite element computation of the stress field around microcracks

Since high-cycle fatigue is considered, the stress fields are calculated in elasticity using CASTEM FE code. The general structure consists in a circular multicrystal containing a crack and embedded in a large homogeneous square plate on which borders the global reversed shear loading is applied, Fig. 3. The polycrystalline structure was simulated by an aggregate of at least 30 grains of definite orientation (denoted by three Euler angles, ϕ_1, ϕ, ϕ_2). The elastic constants for austenite grains are taken as: $C_{11} = 197{,}5$ GPa, $C_{12} = 122$ GPa and $C_{44} = 125$ GPa [9]. Those of the homogeneous medium surrounding the polycrystal are $E = 210$ GPa and $\nu = 0.3$. The mesh was refined in the grains containing and specially near the crack tip in order to capture the associated stress concentration and gradient. Crystallographic orientations were randomly assigned, except for the grains across which the crack propagates.

Since Stage I crystallographic propagation in a FCC metal due to mixed mode I+II loading is modelled, the crack follows {111} planes and its front is supposed to be normal to a $\langle -1\ 1\ 0 \rangle$ direction, so that the dislocations emitted at its tips have a pure edge character.

Table 1 defines the simulated crack paths, that is: the orientations of the {111} planes of the grains along its path (the angle denotes the inclination of the crack plane relative to one of the maximum shear stress planes).

Fig. 4a shows an example of computed shear stress profile between a crack tip and the closest GB. Such computed profiles are used as input for the simulations of crack tip plasticity based on DDD. Fig. 4b represents the same profile plotted versus $1/x$ shows the existence of a K-dominance zone. The mode I and mode II stress intensity factors (SIF) (used in DDD simulations in the criterion for dislocation emission at the crack tip), are determined as the limit of $\sqrt{2\pi x}\sigma_{xx}$ and $\sqrt{2\pi x}\sigma_{xy}$, respectively, as x goes to zero (where x denotes the abscissa in a coordinate system centred at the crack tip with its first axis tangent to the local crack direction). Due to crack roughness and elastic interactions between neighbouring grains, some normal compressive stress can be induced along the crack flank even in the absence of any macroscopic compression. Unilateral contact conditions were thus imposed (in a paragraph below, crack flanks friction is taken into account).

Since cyclic loading is considered, the profile of σ_{xy} in the crack plane and the SIFs are computed under maximum and minimum global stresses. Even under fully reversed shear loading, the loading path undergone by a tortuous

Table 1
Definition of the crack paths

	Grain 1 (°)	Grain 2 (°)	Grain 3 (°)	Grain 4 (°)
Path 1	0	−2	1.5	−5
Path 2	0	−10	5	−10
Path 3	0	−20	10	−10
Path 4	0	−35	20	
Path 5	0	−45		

The angles denote the inclination of the crack plane relative to one of the maximum shear stress planes.

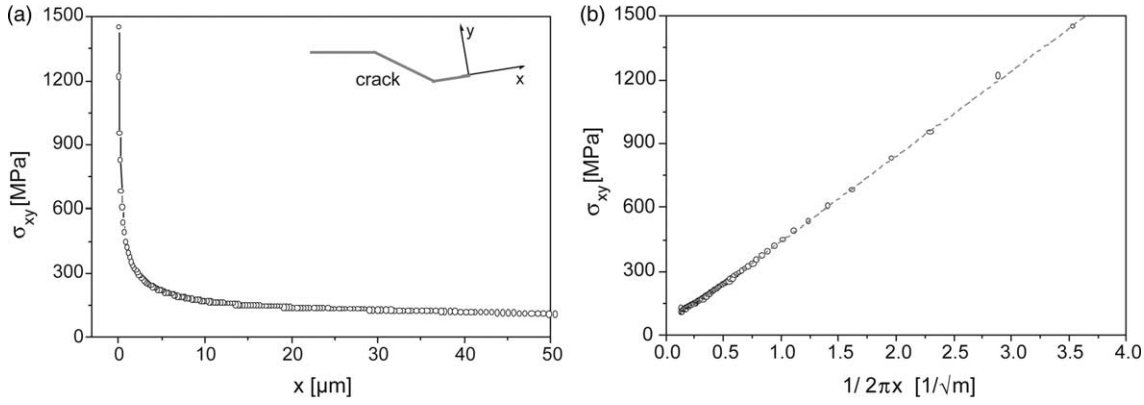

Fig. 4. Typical shape of σ_{xy} profile at the crack tip.

crack is not symmetrical but is constituted with one segment in mixed mode I+II, when the crack tip is open, and one segment in pure shear, when the tip is closed by normal compression (Fig. 5).

The mode I component is considered to assist crystallographic crack propagation when it is present (through its influence on dislocation emission as explained below, or an attenuation of crack flanks friction) but not to drive it. In other words, only coplanar slip is activated by the mode II component, mode I opening being purely elastic.

3.2. Estimation of transgranular crack growth rates by dislocations dynamics

The expression of the stress field generated by a dislocation in an anisotropic elastic medium can be found (see for example Okasaki et al. [10]) after the resolution of a bicubic equation whose coefficients depend on the elastic constants, the slip plane and the slip direction. For an infinite edge dislocation lying along the $(1-1\ 2)$ direction (that is: parallel to the crack front) with a Burgers vector $b = a/2\ (1\ 1\ 0)$ in a FCC crystal, the in-plane shear component is of the form: $Ab/2\pi x$, where A is a constant which depends on the roots of the bicubic equation. In the present case, the value of A was found to be 107 GPa. The A constant would reduce to $\nu(1-\nu)$ for an isotropic elastic medium. The critical mode II stress intensity factor for the emission of a coplanar edge dislocation from the crack tip is calculated as a function of the mode mixity parameter Ψ

$$K_{\mathrm{II}}^{\mathrm{nucl}} = \sqrt{2A\left(\gamma_{\mathrm{us}}^{r} - \alpha\left(\gamma_{\mathrm{us}}^{u} - \gamma_{\mathrm{us}}^{r}\right)\left(\frac{\pi}{2} - \psi\right)\right)} \tag{1}$$

$$\psi = \arctan\left(\frac{K_{\mathrm{II}}}{K_{\mathrm{I}}}\right)$$

where α, γ_{us}^{u} and γ_{us}^{r} are materials parameters. Since, $\gamma_{\mathrm{us}}^{u} > \gamma_{\mathrm{us}}^{r}$, Eq. (1) predicts a lower threshold stress intensity factor for dislocation nucleation when Ψ decreases, that is, when an opening stress is present (for more details, see Sun, Beltz and Rice [11]).

In an isotropic medium, the shear stress on the ith dislocation at abscissa x_{I} zone can, according to Ohr [12] be evaluated as

$$\tau_i = \sigma_{xy}(x_i) - \frac{\mu b_i}{4\pi(1-\nu)x_i} - \sum_{j\neq i}\frac{\mu b_j}{2\pi(1-\nu)}\sqrt{\frac{x_j}{x_i}}\left(\frac{1}{x_j - x}\right)$$

The same equation is assumed to hold in the present case if the term $\mu(1-\nu)$ *is replaced by the constant A*

$$\tau_i = \sigma_{xy}(x_i) - \frac{Ab_i}{4\pi x} - \sum_{j\neq i}\frac{Ab_j}{2\pi}\sqrt{\frac{x_j}{x_i}}\left(\frac{1}{x_j - x_i}\right) \tag{2}$$

in which the three terms represent respectively the shear stress distribution ahead of the crack computed by FE, the image stress (the crack flanks are free surfaces) and

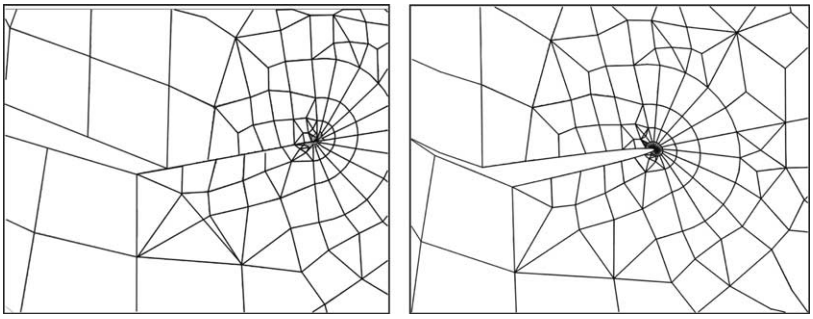

Fig. 5. Deformed mesh showing the crack tip a, close or b, open depending of the applied load direction.

the stress field of other dislocations. Strictly, this equation (as well as Eq. (4) below) is valid for a semi-infinite crack. For a crack of finite length, different expressions have to be used (see for example Tanaka et al. [1]). However, in the present case it has been checked that the difference in predicted crack growth rates, considering finite length or not, is no more than 14% for the smallest crack considered here.

The velocity of each dislocation is calculated (noting the positive part of a number by square brackets) as

$$v_i = v_0 \frac{b_i \tau_i}{|b_i \tau_i|} \left(\frac{\langle |\tau_i| - \tau_f \rangle}{\tau_o} \right)^m \tag{3}$$

where τ_f is the lattice resistance to dislocation glide, v_0 and m two constants (without any influence for the frequencies used in classical fatigue tests) and $\tau_0 = 1$ MPa.

The new position of each dislocation is then deduced, and annihilation criteria checked: if a dislocation comes close enough to the crack tip (less than 0.1 nm) or to a dislocation of opposite sign (less than 16 nm), it is removed from the simulation.

The real mode II stress intensity factor, allowance made for crack tip shielding by the dislocation stress field is then evaluated as

$$K_{II}^{tip} = K_{II} - \sum_{i=1}^{n} \frac{A b_i}{\sqrt{2\pi x_i}} \tag{4}$$

Here again, an equation established for isotropic media by Lin and Thomson [13] has been modified (the term $\mu(1-\nu)$ *is replaced by the constant A*) to take into account crystalline anisotropy.

The dislocation emission criterion

$$K_{II}^{tip} \leq -K_{II}^{nucl} \quad \text{or} \quad K_{II}^{tip} \geq K_{II}^{nucl} \tag{5}$$

is checked to decide whether a negative or positive dislocation can be emitted.

This sequence is repeated until the second cycle is completed. Then, the crack growth rate per cycle is computed. The crack is considered to grow by a fraction β of a Burgers vector each time a pair of positive–negative dislocation has been emitted at the crack tip or when a positive (or negative) dislocation returns to the crack tip. In the latter case, it is assumed that even though the crack tip geometry before the dislocation nucleation is, in principle, recovered when this dislocation comes back, the free surface increment created at nucleation, that has been exposed to environment and gas adsorption in the meantime, will not heal up completely. In addition, both events correspond to some cyclic plastic flow at the crack tip and should thus contribute to some crack growth. The irreversibility factor, β, should probably depend on the environment (because the degree of gas adsorption on fresh metal surfaces should influence the growth rate) and perhaps also on the opening stress along the slip plane (a tensile stress might, to some extent, inhibit healing). It should be best identified from crystallographic crack growth experiments on single crystals. Since such experiments have not been performed yet, β was temporarily fixed to one. It will be shown below that this first-approach assumption of complete irreversibility is too strong.

A continuous DDD simulation of crack growth across a whole grain (tens of microns wide) is out of reach in terms of computation time, since hundreds or even thousands of cycles are needed, for growth rates ranging from one to a hundred Burgers vectors per cycle. So, the transgranular crack growth rate is evaluated independently by DDD for five–six discrete crack lengths per grain.

3.3. Crack growth across grain boundaries

The mechanisms of slip transfer across a grain boundary has been studied by several authors by in situ tests in TEM [14,15]. It seems that direct dislocation transfer is possible only in few cases, provided specific conditions on the type of grain boundary, slip planes and slip directions relative orientation in neighbouring grains are satisfied. In the present model grain boundaries are treated as impenetrable obstacles for the dislocations emitted by the crack. This implies crack deceleration and arrest, unless a source is activated in the next grain, which, after an incubation period could initiate a crack that would link with the arrested one, thus allowing further propagation.

The stress concentration due to the pile up, likely to promote source activation in the next grain has to be estimated. Unfortunately, to the author's knowledge, no exact expression is available in a heterogeneous anisotropic material. However, Head [16] has shown that a screw dislocation of Burgers vector b in a semi-infinite isotropic medium of shear modulus μ_1 close and parallel to an interface with a different elastic isotropic medium, of modulus μ_2, generates in this medium the same stress field as a dislocation of Burgers vector $2\mu_1 b/(\mu_1 + \mu_2)$. Head also indicates that this is a reasonable approximation (maximum error 15%) for an edge dislocation. In the present case (edge dislocations in anisotropic media) an additional (pseudo-isotropic) approximation is made: the in-plane shear moduli of the grain containing the crack tip and that of his neighbour are computed in the coordinate system tangent to the crack tip, and the stress field in the next grain due to the dislocations piled up on the GB is approximated with head's formula.

The resolved shear stresses on a potential source of the next grain, located 1 μm from the GB, is computed as follows. The pileup stress field is added to the elastic stress field computed by FE in the polycrystal without a crack (denoted by $\tau_{polycrystal}$) and to the extra stress due to the presence of the crack ($\tau_{singularity}$, obtained as the difference between the resolved shear stress computed on the source in the cracked elastic polycrystal and in the polycrystal without a crack). But the latter term is weighted by $K_{II}^{tip}/K_{II}^{nom}$ to allow for dislocation shielding of the crack

singularity. Summing up

$$\tau_{\text{resolved}} = \tau_{\text{pileup}} + \tau_{\text{polycrystal}} + \frac{K_{\text{II}}^{\text{tip}}}{K_{\text{II}}^{\text{nom}}}\tau_{\text{singulariy}} \quad (6)$$

The validity of this formula can be illustrated by two limit cases. If the loading range is too small for the crack to emit dislocations (fully elastic case), the last term is equal to $\tau_{\text{singularity}}$, the first one is zero and the total is just the resolved shear stress on the source in the cracked elastic polycrystal. If, at the contrary, the crack tip singularity is completely shielded by dislocations (as in Bilby, Cottrell and Swinden's model), the last term drops and the result is the shear stress in a polycrystal with a slip band impinging a GB.

Only the potential slip systems of the next grain which do not imply a twist of the crack plane (or, in other words, whose normal belongs to the free surface) are considered. There are two reasons for this condition: first, the experimental work of Zhai et al. [7] has shown that the path most likely to be followed by the crack is generally the one which minimises its twist deflection and second, the 2D nature of the model would not allow the description of 3D tortuosity of the crack path.

If one of the computed resolved shear stresses range $\Delta\tau_{\text{res}}$ exceeds a critical value, $\Delta\tau_{\text{s}}$, a source is considered to be activated.

Although, as explained in the introduction, it seems clear that the transfer of a crack tip beyond a GB does not coincide with the activation of a slip system but may require a maturation period, the precise physical mechanisms of Stage I fatigue cracks crossing grain boundaries are far from being understood yet and are likely to vary with the characteristics of the grain boundaries. Well designed experiments on bi-crystals as well as simulations at a fine scale, like molecular dynamics are needed.

That is why only an empirical 'good sense' evaluation of the number of cycles, N_{inc}, for crack growth beyond the grain boundary, once a source has been activated can be proposed. The higher the range of the resolved shear stress on this source, the sooner resulting cyclic plasticity should initiate a microcrack and the faster this microcrack should merge with the arrested crack, thus permitting further crack growth. Now, the resolved shear stress range on the source keeps varying as the crack approaches (it is evaluated during each of the five (or six) DDD simulations performed in each grain and it is linearly interpolated for intermediated crack lengths). That is why the incubation period is obtained from an integral equation and is considered elapsed when

$$\int_{N_{\text{activation}}}^{N_{\text{activation}}+N_{\text{incubation}}} C(\Delta\tau_{\text{res}}(N) - \Delta\tau_{\text{s}})^n \mathrm{d}N = 1 \quad (7)$$

where C and n are constants to be determined from experimental data on short cracks kinetics. Eq. (7) was inspired from the incubation model of Morris et al. [6]. When condition (7) is verified, a new mesh with a 1 μm long branch-crack along the activated slip plane in the next grain is generated and the whole process starts again.

Table 2
Parameters used in the simulations

γ_{us}^{u} [J.m^{-2}]	γ_{us}^{r} [J.m^{-2}]	τ_{f} [MPa]	τ_{s} [MPa]	C [MPa$^{1/n}$]	N	β
1.64	1.41	58	82	1.5×10^{-10}	2	1

3.4. Parameters of the simulation

The numerical values of the materials parameters used for the simulations are gathered in Table 2. The resistance of the crystal to dislocation glide, τ_{f}, was set at 58 MPa, the saturation shear stress measured by Kaneko et al. [17] in an austenitic stainless steel single crystal oriented for single glide and submitted to cyclic loading in the range where localized slip bands form.

The measured micro-yield stress in shear of the material is $\tau_y = 92$ MPa (for a plastic strain $\gamma_{\text{p}} = 10^{-5}$). According to FE simulations of the stress field in a polycrystal, the resolved shear stress on the most favourably oriented slip system is only 83% of the macroscopic shear stress (due to the shear modulus of the most favourably oriented grain, which is smaller than the average modulus). The critical shear stress for source activation, τ_{s} was thus estimated as $\tau_{\text{s}} = 0.83\ \tau_y = 82$ MPa (the shear stress range for cyclic plasticity at the source is then $\Delta\tau_{\text{s}} = 2\ \tau_{\text{s}}$).

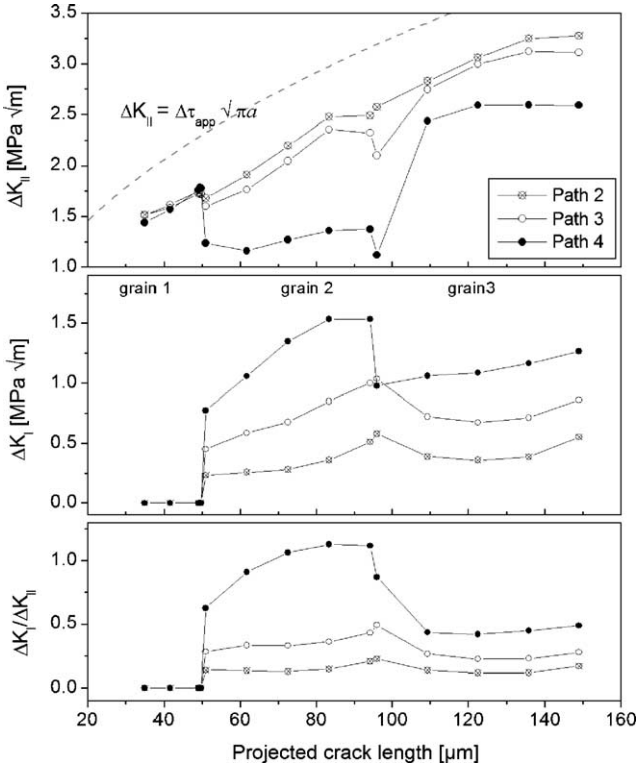

Fig. 6. Computed evolution of SIFs for three different crack paths.

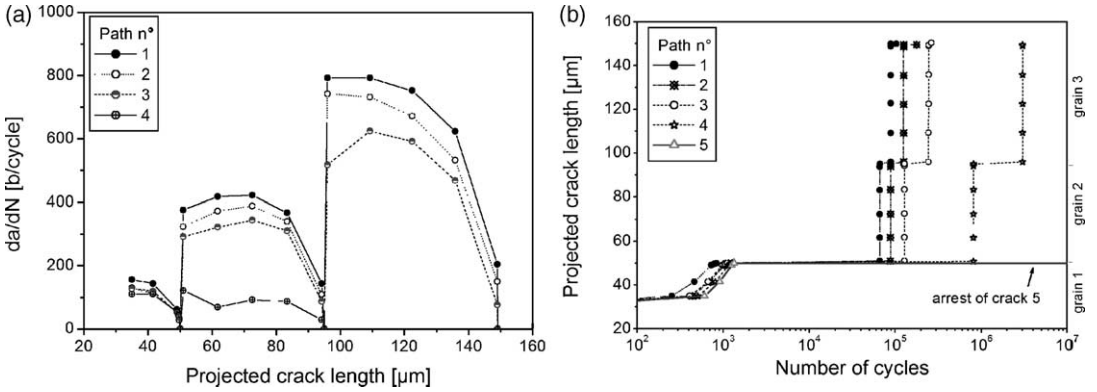

Fig. 7. Predicted kinetics for four different crack paths: a, da/dN versus projected crack lengths and b, projected crack lengths versus number of cycles.

The parameters γ_{us}^{u}, γ_{us}^{r} and α have to be determined through atomic-scale simulations that were not attempted in the present study. γ_{us}^{u} was chosen so that the dislocation emission threshold in pure shear is 0.55 MPam, which gives a threshold for crystallographic crack growth under fully reversed shear loading of 1.1 MPam, the order of magnitude measured on single crystals of FCC structure [18,19], also in agreement with measurements on 316L polycrystals by Blochwitz et al. [20]. The parameter α and the ratio $\gamma_{us}^{r}/\gamma_{us}^{u}$ were chosen in the range reported by Sun et al. [11] for Fe, Ni and Al.

The coefficients C and n were adjusted so that the range of computed arrest periods on GBs was in agreement with our experimental data on short cracks kinetics.

Unless specified, the applied shear stress is ± 130 MPa and the mean grain size 50 μm. For sake of simplicity, one tip of the crack is arrested by an impenetrable GB (thanks to an appropriate choice of Euler angles in the neighbouring grain) so that only one tip has to be monitored. The crack length (projected along the maximum shear stress plane) $2a$ increases from 35 to 150 μm.

4. Simulations results

The evolution of the computed SIFs and mode mixity ratio with microcracks length (projected on the maximum shear plane) for the crack paths described in Table 1 are plotted on Fig. 6. The evolution of ΔK_{II} obtained using a straight-crack uniform stress approximation $\left(\Delta K_{II}^{app} = \Delta\tau_{app}\sqrt{\pi a}\right)$ is also reported for comparison.

It appears that this approximation systematically overestimates ΔK_{II} because the most favourable grain orientation for crack initiation corresponds to a shear modulus which is only 83% of the average modulus on the one side, and the above-mentioned approximation is for a straight crack, whereas roughness shields the crack tip singularity, on the other side. Furthermore, ΔK_{II} is highly variable from one microcrack to the other, depending on their paths. It does not systematically increase with the crack length but it may exhibit a sudden drop due to tilting at a GB that can lead to crack arrest. The scatter in ΔK_{I} is even wider than in ΔK_{II}. ΔK_{I} also shows abrupt variations at GBs.

With such a wide scatter in the mechanical conditions—merely due to the variability of local texture in the polycrystal—the scatter in experimental data on microcracks growth and fatigue lives is not surprising.

Fig. 7a compares the evolution of the growth rates and Fig. 7b the evolution of the projected lengths for the different crack paths described in Table 1. The latter is consistent with the experimental microcrack growth kinetics plotted on Fig. 1. The predicted scatter is as important, as the measured scatter.

For a given path, the incubation period due to GBs is smaller and smaller as the crack grows and is almost zero beyond the third GB, which is also consistent with experimental observations. Crack $n°5$ cannot cross the first GB, due to a high tilt angle (45°). The fastest crack growth corresponds to the smallest tilt angles and thus the smallest roughness (crack path $n°1$). This suggests that the local texture has an essential influence on the endurance limit.

The influence of the stress range is illustrated on Fig. 8 that mimics a Wohlers plot. The number of cycles needed to develop a crack, twice the mean grain size in length varies a lot with the crack path. Note that the scatter in lives increases as the stress range decreases (for ± 140 MPa,

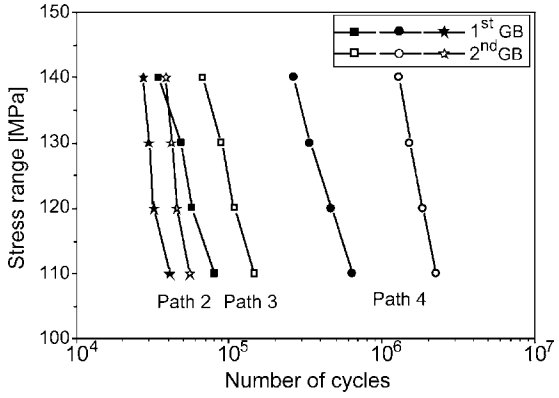

Fig. 8. Pseudo wholer's plot: influence of the stress range on the number of cycles needed to develop a crack, twice the mean grain size in length, along path $n°4$.

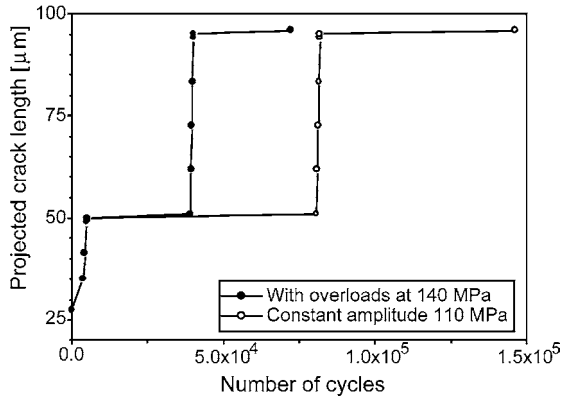

Fig. 9. Influence of a few (45) overload cycles at ± 140 MPa on microcrack growth under ± 110 MPa.

10 times more cycles are needed to cross the first GB for crack path $n°2$ than for $n°4$, whereas for ± 110 MPa, the ratio is 15). This is consistent with experimental observations.

5. Fluctuating stress levels

Many experimental data in the literature show that a few 'large cycles' (in such a small number that their contribution to damage in terms of N/N_f is insignificant) may however enable arrested microcracks to cross GBs, so that cycles with a stress range *below the endurance limit* may become damaging, because it can cause further transgranular crack growth [21]. Such interactions are encountered in aircraft structures submitted to small load fluctuations in flight with a few large cycles corresponding to take-off and landing.

The present model reproduces this fact, as illustrated by Fig. 9. For a normal stress range of ± 110 MPa, 45 overload cycles at ± 140 MPa applied when the crack tip is close to the first and second GB reduce by a factor of two the number of small cycles needed to grow the crack to the third grain.

6. Influence of the 3D shape of cracks and crack flanks friction

The comparison of Figs. 1 and 7 shows that the simulations overestimate transgranular crack growth rates (that do not exceed 10 b/cycle in experiments, but exceed 100 b/cycle in simulations). This might be due to overestimates of SIFs.

The main source of error in the estimation of the crack driving force comes from the 2D model that assumes a through-crack instead of a surface crack. The 3D shape of Stage I cracks can be quite complicated and partly determined by the underlying microstructure. But, as a first attempt, it can be assumed semi-elliptical with a and c as depth and half surface length, respectively. The correction factors that should be applied to K_I and K_{II} values computed on the basis of the surface crack, c, to take into account the 3D aspect can be estimated by the formulas of Newman and Raju [22] and Kassir and Sih [23], respectively. Although the latter is for an elliptical crack in an infinite body, it was shown to provide a reasonable approximation for a semi-elliptical crack in a semi-infinite plate [24] and even in a tubular specimen under torsion [25]. For instance, for $a/c = 1$, 0.5 and 0.25, the correction factors on K_{II} are approximately 0.75, 0.53 and 0.32, respectively.

A second reason for crack driving force overestimation is crack flanks friction, which was neglected in the first simulations but is present, as shown by Fig. 2. To quantify this effect, FE meshes representing the same crack paths as those described in Table 1, but in a large plate of homogeneous elastic medium were prepared and FE simulations of reversed shear cycles were performed, taking crack flanks friction into account through Coulomb's law (with a friction coefficient denoted by f). Fig. 10a shows the evolution of the effective K_{II} at the right tip of a crack with a single tilted portion for various values of f. Since crack flanks contact occurs only in one of the two successive shearing directions (cf. Fig. 5), the crack tip singularity is shielded only during half of the cycle. For a crack with two

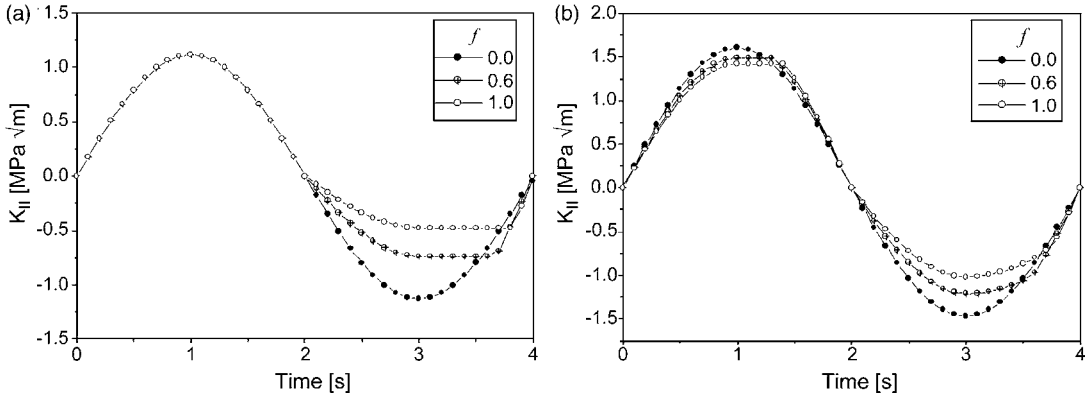

Fig. 10. Evolution of nominal and effective K_{II} over an alternate shear cycle for a crack with: a, a single tilted segment ($\theta = -20°$) and b, two tilted segment ($\theta_1 = -20°$, $\theta_2 = 10°$).

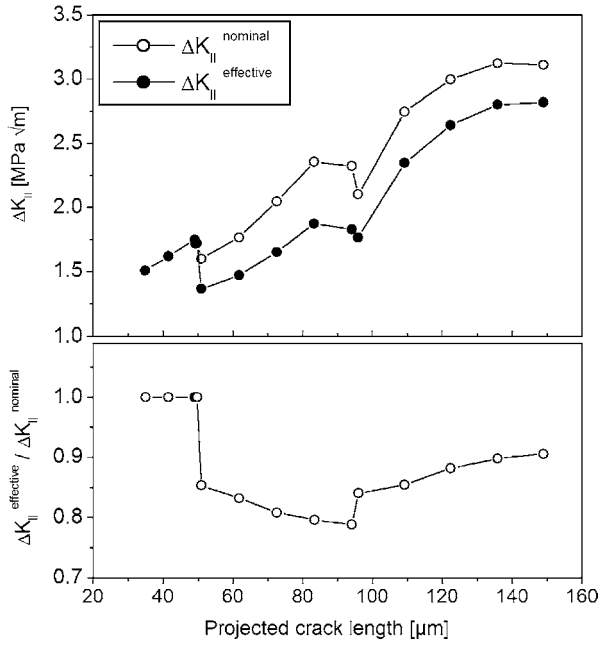

Fig. 11. Influence of crack flanks friction on the evolution of the effective ΔK_{II} along path $n°$ 3 and the mode mixity ratio $\Delta K_I/\Delta K_{II}$ along path $n°3$.

tilted portions (with tilt angles of opposite signs), an attenuation of K_{II} occurs in both parts of the cycle, due to the contact and friction of the second and third crack segment alternatively (Fig. 10b).

Fig. 11 compares the evolution of the nominal and effective ΔK_{II} with the projected crack length for crack paths $n°3$, for a coefficient of friction $f=0.5$ (which seems to be the right order of magnitude for an austenitic stainless steel at 20 °C [26]). $\Delta K_{II}^{effective}$ was approximated by multiplying the nominal ΔK_{II} values computed in the heterogeneous stress field of the polycrystal by the ratio $\Delta K_{II}^{effective}/\Delta K_{II}^{nominal}$ computed for the current crack geometry in the homogeneous medium. When the crack propagates in the second grain (with a tilt angle of $-20°$), $\Delta K_{II}^{effective}/\Delta K_{II}^{nominal}$ decreases progressively. It increases again in the third grain where the tilt angle is $+10°$. Note that the decrease in $\Delta K_{II}^{effective}$ due to friction increases the mode mixity ratio $\Delta K_I/\Delta K_{II}^{effective}$ and should thus favour the transition to Stage II.

Fig. 12 compares the evolution of predicted crack growth rate for path $n°3$ using nominal or effective SIFs. In the latter case, the growth rates are approximately divided by 1.5. The effect of a 3D correction alone (growth rates divided approximately by three, for $a/c=1$) and combined effects of crack flanks friction and 3D correction on crack growth rates are also illustrated.

Even though microcracks are often shallow in torsional fatigue (a/c values as low as 0.14 have been reported), so that 3D corrections on ΔK_{II} could reduce predicted crack growth rates even more, it seems difficult to bring computed and measured transgranular crack growth rates in complete agreement.

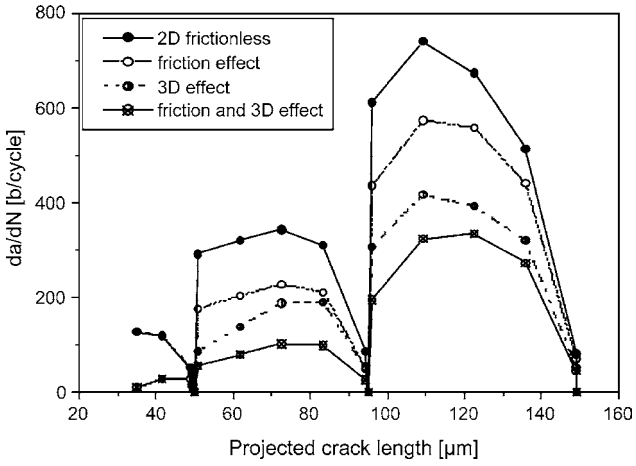

Fig. 12. Influence of the friction correction alone, 3D correction alone ($a/c=1$), or combined 3D and friction corrections on the evolution of the computed crack growth rate along path $n°3$.

The computation of the growth rate from the dislocation flux at the crack tip whith $\beta=1$ (assumption of complete irreversibility of atomic bonds brake) seems, to a large extent, responsible for the overestimation of the growth rate. A much smaller value (a few hundredths) might be more realistic Note however, that the number of cycles spent in transgranular propagation is quite negligible compared to arrest periods, so that this point is not so important in practice.

7. Conclusions

Crystallographic propagation of tortuous fatigue cracks in a polycrystal was modelled using local stresses computed by FE as input for DDD. The driving force on Stage I cracks was shown to be quite different from the apparent value, computed from the applied stress field and neglecting the crack roughness. An incubation period for crack transfer beyond GBs was introduced. The simulations reproduce qualitatively the shape of experimental kinetics, characterized by arrest periods at GBs that decrease as the crack grows. In accordance with experimental observations, it predicts a large scatter in microcracks growth rates and an increased scatter for small loading ranges. It suggests that the local texture has an essential influence on the endurance limit. Transgranular crack growth rates were shown to be reduced substantially by crack flanks friction (by a factor 1.5, for a friction coefficient equal to 0.5). The growth rate also depends strongly on the 3D shape of the crack (approximately 3 times less for a semi-circular crack than for a through-crack). The fact that overloads may suppress the endurance limit by unlocking microcracks arrested at GBs is qualitatively described by the model.

Acknowledgements

The authors acknowledge the support from CEA, CNRS and EDF through CPR SMIRN.

References

[1] Tanaka K, Akiniwa Y. Mechanics of small fatigue crack propagation, in small fatigue cracks. In: Ravichandran KS, Ritchie RO, Murakami Y, editors. Mechanics, mechanisms and applications. Elsevier Science; 1999. p. 59–71.

[2] Wilkinson AJ. Modelling the effects of texture on the statistics of Stage I fatigue crack growth. Philos Mag A 2001;81(4):841–55.

[3] Doquet V. A first stage in the development of micromechanical simulations of the crystallographic propagation of fatigue cracks under multiaxial loading. Fatigue Fract Eng M 1998;21:661–72.

[4] Doquet V. Micromechanical simulations of microstructure-sensitive Stage I fatigue crack growth. Fatigue Fract Eng M 1999;22:215–22.

[5] Ludwig W, Buffière JY, Savelli S, Cloetens P. Study of the interaction of a short fatigue crack with grain boundaries in a cast aluminium alloy using X-ray microtomography. Acta Mater 2003;51(3):585–98.

[6] Morris WL, James MR, Buck O. Growth rate models for short surface cracks in Al 2219-T851. Metall Trans 1981;12A:57–64.

[7] Zhai T, Wilkinson AJ, Martin JW. A crystallographic mechanism for fatigue crack propagation through grain boundaries. Acta Mater 2000; 48:4917–27.

[8] Grummon DS, Jones JW. In: Ritchie RO, Starke EA, editors. The effect of ion beam mixed Ni–Al surface layers on PSB extrusion morphology in fatigued nickel. Fatigue'87: proceedings of the third international fatigue congress, vol. 1. EMAS; 1987. p. 83–92.

[9] Hosford WF. The mechanics of crystals and textured polycrystals. Oxford, New York: Oxford University Press; 1993.

[10] Okazaki M. Analysis of crack tip sliding displacement in anisotropic elastic media and its application to Stage I fatigue crack growth. Metall Trans 1991;22A:479–87.

[11] Sun Y, Beltz GE, Rice JR. Estimates from atomic models of tension–shear coupling in dislocation nucleation from a crack tip. Mater Sci Eng 1993;A170:67–85.

[12] Ohr SM. An electron microscope study of crack tip deformation and its impact on the dislocation theory of fracture. Mater Sci Eng 1985; 72:1–35.

[13] Lin IH, Thomson R. Cleavage, dislocation emission, and shielding for cracks under general loading. Acta Metall 1986;34:187–206.

[14] Lee TC, Robertson IM, Birnbaum HK. TEM in situ deformation study of the interaction of lattice dislocations with grain boundaries in metals. Philos Mag A 1990;62(1):131–53.

[15] Shen Z, Wagoner RH, Clarck AT. Dislocation and grain boundary interaction in metals. Acta Metals 1988;36(12):3231–42.

[16] Head AK. The interaction of dislocations and boundaries. Philos Mag 1952;44(348):92–4.

[17] Kaneko Y, Morita Y, Hashimoto S. Change in shape of hysteresis loop during cyclic deformation on austenitic stainless steel single crystals oriented for single slip. Scripta Mater 1997;7:963–8.

[18] Brown CW, King JE. The relevance of microstructural influences in the short crack regime to overall fatigue resistance. In: Ritchie R, Lankford K, editors. Small fatigue cracks, 1986. p. 73–95.

[19] Tong ZX, Lin S, Hsiao CM. The mechanism of fatigue crack propagation in pure aluminium single crystals. Scripta Metall Mater 1986;20:977–82.

[20] Blochwitz C, Richter R. Plastic strain amplitude dependent surface path of microstructurally short fatigue cracks in face-centred cubic metals. Mater Sci Eng 1999;A267:120–9.

[21] Miller KJ, O'Donnell WJ. The fatigue limit and its elimination. Fatigue Fract Eng M 1999;22:545–57.

[22] Newman JC, Raju IS. Stress intensity factor equations for crack in three-dimensional finite bodies. Eng Fract Mech 1983;1185–92.

[23] Kassir MK, Sih GC. Three-dimensional stress distributions around an elliptical crack under arbitrary loadings. J Appl Mech 1966;33: 601–11.

[24] He MY, Hutchinson JW. Surface crack subjected to mixed-mode loading. Eng Fract Mech 2000;65:1–14.

[25] Doquet V, Mignot F, Frelat J. In: Blom AF, editor. A three-dimensional micromechanical analysis of Stage I fatigue crack growth in reversed torsion. Fatigue'02: Proceedings of the Eighth International Fatigue Congress, vol. IV. EMAS; 2002. p. 2673–80.

[26] Van Herpen A, Reynier B, Phalippou C. Effect of test duration on impact/sliding wear damage of 304L stainless steel at room temperature: metallurgical and micromechanical investigations. Wear 2001;249:37–49.